

## Supporting Information

# **New Particle Formation from the Vapor Phase: From Barrier Controlled Nucleation to the Collisional Limit**

*Kayane K. Dingilian<sup>1†</sup>, Martina Lippe<sup>2†</sup>, Jakub Kubečka<sup>3†</sup>, Jan Krohn<sup>2</sup>, Chenxi Li<sup>2</sup>, Roope Halonen<sup>3</sup>, Fatemeh Keshavarz<sup>3</sup>, Bernhard Reischl<sup>3</sup>, Theo Kurtén<sup>4</sup>, Hanna Vehkamäki<sup>3\*</sup>, Ruth Signorell<sup>2\*</sup>, and Barbara E. Wyslouzil<sup>1,5\*</sup>*

<sup>1</sup>William G. Lowrie Department of Chemical and Biomolecular Engineering, The Ohio State University, Columbus, Ohio 43210, USA

<sup>2</sup>Department of Chemistry and Applied Biosciences, ETH Zürich, Vladimir-Prelog-Weg2, 8093 Zürich, Switzerland

<sup>3</sup>Institute for Atmospheric and Earth System Research / Physics, University of Helsinki, P.O. Box 64, FI-00014, Helsinki, Finland

<sup>4</sup>Department of Chemistry, Faculty of Science, University of Helsinki, FI-00014, Finland

<sup>5</sup>Department of Chemistry and Biochemistry, The Ohio State University, Columbus, Ohio 43210, USA

<sup>†</sup>Equal author contribution

\*corresponding authors: [hanna.vehkamaki@helsinki.fi](mailto:hanna.vehkamaki@helsinki.fi); [rsignorell@ethz.ch](mailto:rsignorell@ethz.ch); [wyslouzil.1@osu.edu](mailto:wyslouzil.1@osu.edu)

## S1. Further Experimental Details

### A. Experimental Setup and Data Processing – Ohio State University

The continuous flow experimental setup and the supersonic nozzle used here (Nozzle T3\_CaF2) are described in detail in the literature<sup>1-5</sup>. To summarize briefly, liquid argon (99.998% purity) and carbon dioxide (99.9% purity, maximum water level of 10 ppm) were purchased from Praxair. Before starting an experiment, the system was purged with argon at a flow rate of 90 standard liters per minute (SLM) for 1 hour to minimize contamination. During an experiment, gaseous Ar and CO<sub>2</sub> are drawn from their respective sources and brought to room temperature by inline heaters. The pressure at each source is maintained by a regulator, and the flows are controlled by mass flow controllers (Ar: MKS 1559 300 SLM; CO<sub>2</sub>: MKS GE50A 3.8 SLM). After combining the gases, the temperature of the flowing stream is adjusted to maintain the desired stagnation temperature  $T_0$  in the plenum using a circulating water bath. The stagnation pressure  $p_0$  is based on the static pressure  $p$  measured in the nozzle sidewall upstream of the converging section of the nozzle that is corrected for the momentum of the flow. A movable static pressure probe, located along the centerline of the nozzle, is used to obtain the axial pressure profile with measurements starting a few cm upstream of the throat and ending ~10 cm downstream of the throat.

After measuring pressure traces for pure Ar (dry trace) and the Ar-CO<sub>2</sub> mixtures (wet traces), the other properties of the condensing flow are determined by integrating the four governing equations describing supersonic flow in the presence of heat addition. The measured variables used as input to the integration include  $p$  from the wet trace and the area ratio  $A/A^*$  from the dry trace. Integration yields position-resolved temperature  $T(z)$ , density  $\rho(z)$ , velocity  $u(z)$ , and condensate mass fraction  $g(z)$  profiles for the condensing flow where  $z$  is the position relative to the throat.

These values then yield the supersaturation profile  $S(z)$  for  $\text{CO}_2$ . Position resolved measurements are converted to time ( $t$ ) resolved measurements using  $dt = dz/u$ , and a theoretical nucleation rate profile  $J_{\text{theory}}(t)$  is calculated based on  $S(t)$  and  $T(t)$ . The  $J_{\text{theory}}(t)$  profile is used to characterize the conditions yielding the maximum nucleation rate and the time over which most of the particles were formed,  $\Delta t$ .<sup>1</sup> The values of the partial pressure of  $\text{CO}_2$  ( $p_{\text{CO}_2}$ ) and the temperature corresponding to the peak nucleation rate are reported in Table S1.

Aerosol number densities  $N$  are normally determined via *in situ* small angle X-ray scattering measurements using the Advanced Photon Source at Argonne National Laboratory. This was done for the experiments reported in Dingilian *et al.*<sup>1</sup>, but for the new low  $\text{CO}_2$  concentration measurements reported as part of this work, access to the synchrotron was not possible for our complex experiment. Thus, the values of  $N$  used to determine the nucleation rates were estimated by extrapolating the data at higher partial pressures<sup>1</sup> to the current conditions. The data and fit used in the extrapolation are available as figures 4.28 and 4.29 of Dingilian<sup>6</sup>. The experimental nucleation rates  $J_{\text{exp}}$  were then calculated as

$$J_{\text{exp}} = \frac{N}{\Delta t} \times \frac{\rho_{\text{NZ}}}{\rho_{\text{VV}}}, \quad (\text{S1})$$

where the density ratio corrects for any difference in the density of the flow between the nucleation zone (NZ) and the SAXS viewing volume. The values of  $J_{\text{exp}}$  measured as part of this work are reported in Table S1, and for completeness, the data published previously by Dingilian *et al.*<sup>1</sup> are also included.

**Table S1:** A summary of the current and previously published <sup>1</sup> OSU experimental results includes the conditions prior to the expansion (Stagnation conditions), those corresponding to the peak nucleation rates (Onset conditions), and the nucleation rates. The latter include the experimentally measured rate  $J_{\text{exp}}$ , the correction factor that accounts for incomplete thermalization of the clusters  $f$  (Section S1.C) and the nucleation rates,  $J = J_{\text{exp}}/f$ . Here, the mol % CO<sub>2</sub> and  $p_{\text{CO}_2,0}$  are the initial concentration and pressure of CO<sub>2</sub>, and  $p_{\text{CO}_2}$  and  $T$  are the condensable pressure and the temperature corresponding to the peak nucleation rate. All experiments started from  $T_0 = 293.15$  K and total stagnation pressure for (CO<sub>2</sub> + Ar) of  $p_0 = 61.15$  kPa.

Current Experimental Results						
Stagnation conditions		Onset conditions		Nucleation rates		
mol % CO <sub>2</sub>	$p_{\text{CO}_2,0}$ [Pa]	$p_{\text{CO}_2}$ [Pa]	$T$ [K]	$J_{\text{exp}}$ [cm <sup>-3</sup> s <sup>-1</sup> ]	$f$	$J$ [cm <sup>-3</sup> s <sup>-1</sup> ]
0.5	305	7.14	65.8	$6.06 \times 10^{17}$	0.393	$1.54 \times 10^{18}$
0.5	305	7.45	66.5	$6.15 \times 10^{17}$	0.391	$1.57 \times 10^{18}$
0.7	427	10.8	68.8	$6.01 \times 10^{17}$	0.327	$1.84 \times 10^{18}$
0.85	519	13.3	69.6	$4.62 \times 10^{17}$	0.290	$1.59 \times 10^{18}$
1	611	14.7	67.6	$3.79 \times 10^{17}$	0.256	$1.48 \times 10^{18}$
1	611	15.6	70.7	$4.31 \times 10^{17}$	0.261	$1.65 \times 10^{18}$
1.2	733	21.5	73.4	$4.21 \times 10^{17}$	0.237	$1.77 \times 10^{18}$
1.5	916	28.9	75.8	$6.27 \times 10^{17}$	0.206	$3.04 \times 10^{18}$
1.7	1038	33.9	76.5	$5.82 \times 10^{17}$	0.190	$3.07 \times 10^{18}$
2	1221	38.6	75.1	$3.52 \times 10^{17}$	0.165	$2.13 \times 10^{18}$
2	1221	41.5	79.2	$4.28 \times 10^{17}$	0.170	$2.52 \times 10^{18}$
2	1221	41.5	78.1	$5.45 \times 10^{17}$	0.170	$3.21 \times 10^{18}$

Prior results of Dingilian <i>et al.</i> <sup>1</sup>						
Stagnation conditions		Onset conditions		Nucleation rates		
mol % CO <sub>2</sub>	$p_{\text{CO}_2,0}$ [Pa]	$p_{\text{CO}_2}$ [Pa]	$T$ [K]	$J_{\text{exp}}$ [cm <sup>-3</sup> s <sup>-1</sup> ]	$f$	$J$ [cm <sup>-3</sup> s <sup>-1</sup> ]
3.0	1800	61	77.8	$3.94 \times 10^{17}$	0.123	$3.21 \times 10^{18}$
3.0	1800	63	78.2	$6.01 \times 10^{17}$	0.123	$4.87 \times 10^{18}$
6.0	3700	134	82.0	$5.62 \times 10^{17}$	0.072	$7.81 \times 10^{18}$
9.0	5500	198	82.5	<sup>a</sup> $5.95 \times 10^{17}$	0.052	$1.14 \times 10^{19}$
12.0	7330	281	86.0	$5.21 \times 10^{17}$	0.041	$1.27 \times 10^{19}$
12.0	7330	278	85.7	$5.14 \times 10^{17}$	0.041	$1.26 \times 10^{19}$
15.0	9160	345	86.2	<sup>a</sup> $5.22 \times 10^{17}$	0.034	$1.53 \times 10^{19}$
18.0	10991	411	87.2	$5.55 \times 10^{17}$	0.029	$1.91 \times 10^{19}$
18.0	10991	408	87.6	$3.98 \times 10^{17}$	0.029	$1.37 \times 10^{19}$
24.0	14700	528	88.4	$3.09 \times 10^{17}$	0.023	$1.37 \times 10^{19}$
31.2	19100	701	91.9	$2.31 \times 10^{17}$	0.018	$1.27 \times 10^{19}$
38.9	23800	770	91.7	$2.04 \times 10^{17}$	0.015	$1.38 \times 10^{19}$
39.3	24000	793	92.3	$2.16 \times 10^{17}$	0.015	$1.47 \times 10^{19}$

a. based on measurements made at a fixed position in the nozzle and corrected for coagulation - see Table 2 in Dingilian *et al.* <sup>1</sup>.

## B. Experimental Setup and Data Processing – ETH Zurich

The experimental setup in Zurich has been discussed in detail in our previous publications (see <sup>7-13</sup>). To summarize, we use mass flow controllers to regulate the flow of the condensable gas (carbon dioxide, PanGas 4.5) and the carrier gases (argon, PanGas 5.0, nitrogen, PanGas 5.0 and methane, Messer 5.5). Methane is also used as an internal standard. Two feeding valves with a repetition rate of 20 Hz and an opening time of 6  $\mu$ s are used to supply the gas mixture to the so-called stagnation volume with stagnation temperature  $T_0$  and stagnation pressure  $p_0$ . The gas mixture is then expanded through the Laval nozzle generating a uniform flow at the nozzle exit with temperature  $T$ , CO<sub>2</sub> pressure  $p_{\text{CO}_2}$  and carrier gas pressure  $p_{\text{car}}$ .

The flow uniformity is extended into the post-nozzle flow region ( $\sim 100$  mm in length) by matching the pressure in the background to  $p_{\text{CO}_2} + p_{\text{car}}$ . The Laval nozzle is fixed on a linear translation stage, which enables us to change the axial distance  $z'$ , i.e. the distance between nozzle exit and skimmer (see Figure 1, main text). A change in  $z'$  leads to a change in nucleation time  $t$  with a resolution of  $\sim 2 \mu\text{s}$ .

We determine the Mach number and temperature from measurements of the stagnation and impact pressures  $p_0$  and  $p_I$ , respectively, using the Rayleigh-Pitot equation and assuming isentropic flow conditions and ideal gas behavior (see refs. 8, 10-12 for more information). We usually record 20-40 measurements of  $p_0$  and  $p_I$  at a given  $z'$ . From this, the axially averaged Mach number  $M$  and temperature  $T$  can be determined with standard deviation  $\sigma$  (Table S2).

A skimmer (Beam Dynamics, 1 mm in diameter) is used to sample the core of the post-nozzle flow. The clusters are then ionized with single photons at 13.8 eV (89.8 nm) generated by a two-color-four-wave mixing process in a krypton expansion at 20 Hz using a home-built table-top vacuum ultraviolet (VUV) laser. Single-photon ionization has been proven to be a soft ionization method for weakly-bound clusters (see refs. 14-18 and references therein). After ionization, the clusters are accelerated by a Wiley McLaren type mass spectrometer using voltages up to 30 kV. These high voltages lead to a high dynamic mass range and high sensitivity of our measurements. The clusters are finally detected by a microchannel plate (MCP) detector. The monomer is usually  $10^3$ - $10^4$  times more abundant than the clusters. We therefore record the monomer and clusters in separate measurements using different experimental settings. Additionally, the monomer is deflected by a pulsed plate (see refs. 7 and 12 for more information) during the cluster measurements to avoid saturation effects on the MCP.

We use the experimental setup to record two types of data (see also main text): i) nucleation onset measurements (Tables S2) and ii) nucleation rate measurements (Table S3). Onset is determined at a fixed position in the flow by finding the conditions where a rapid increase in the maximum (or mean) cluster size is observed for a small increase in condensable partial pressure ( $\sim 0.1\%$ ) or decrease in temperature ( $\sim 0.4$  K). As described in more detail below, nucleation rates are determined by measuring the increase in cluster number as a function of position, or equivalently time, in the post-nozzle flow. The thermodynamic requirement of nucleation is that the supersaturation  $S = p_{\text{CO}_2}/p_{\text{CO}_2}^{\text{eq}}(T)$  is greater than one (supersaturation), where  $p_{\text{CO}_2}$  is the partial pressure of  $\text{CO}_2$  and  $p_{\text{CO}_2}^{\text{eq}}(T)$  is the equilibrium vapor pressure of  $\text{CO}_2$ . However, nucleation can only be observed if enough particles nucleate in the time accessible by the experiment. To account for this, we refer to conditions where the  $S > 1$  but nucleation is not observed as *subcritical* conditions and to conditions where nucleation has already taken place as *supercritical* conditions. To observe the onset of nucleation, the experimental conditions must be systematically tuned to explore the range from subcritical to supercritical conditions. These fine steps were achieved by changing  $T$  at a given  $p_{\text{CO}_2}$  and  $z'$  (60 mm for all measurements in Table S2), which was realized by replacing parts of the argon carrier gas by either methane or nitrogen. This leads to an increase in  $T$  and therefore to a decrease in  $S$ . As mentioned in the main text, a decrease of  $T$  of  $\sim 0.4$  K is enough to change from supercritical to subcritical conditions (see refs. 10 and 11). We identify the conditions at which the first supercritical mass spectrum is recorded as nucleation onset. The different onset conditions are given in Tables S2 and S3.

The recording and analysis of mass spectra to determine nucleation rates has been described in detail in refs. 7, 12-13. In this experiment, we record mass spectra at a constant  $S$  as a function of

$t$ , and add a small amount of methane as an internal standard to the gas mixture. As outlined in refs. 7 and 12, we can determine the number concentrations of the clusters,  $N_n$ , by:

$$N_n = \frac{I_n \cdot \sigma_{\text{CH}_4} \cdot N^{\text{CH}_4}}{I_{\text{CH}_4} \cdot \sigma_{\text{CO}_2} \cdot n} \quad (\text{S2})$$

$I_n$  and  $I_{\text{CH}_4}$  are the integrated ion signals of cluster  $n$  and  $\text{CH}_4$ , respectively,  $\sigma_{\text{CO}_2}$  and  $\sigma_{\text{CH}_4}$  are the respective monomer photoionization cross sections of  $\text{CO}_2$ <sup>19</sup> and  $\text{CH}_4$ <sup>20</sup>. The uncertainty on  $N_n$  is estimated to be a factor of  $\sim 5$  (see refs. 7, 12-13).

At early nucleation times, monomer depletion and more complex growth mechanisms such as coagulation can be neglected because the monomer abundance is  $10^{3-4}$  times higher than that of the clusters. Under these conditions, the total cluster concentration summed over all clusters larger than a critical size  $n^*$  ( $n > n^*$ ),  $N_{\text{cluster,tot} > n^*}$ , as a function of  $t$  gives direct access to the nucleation rate  $J_{\text{exp}}$  by using eq. 2 in the main text.

More details are provided in refs. 7 and 12. For simplicity, we choose  $n^* = 1$ . Note that the choice of  $n^*$  has only minor influence on  $J_{\text{exp}}$ . We estimate the relative uncertainty of  $J_{\text{exp}}$  to be a factor of 2 and the absolute uncertainty to be an order of magnitude (see refs. 7, 12-13). The experimental conditions for the nucleation rate measurements are given in Table S3. Note that these data were previously published in refs. 7 and 21.



**Table S2:** Experimental parameters of the onset measurements performed at ETH Zurich. The data in the last row were first published in ref. 21. Further onset data retrieved from our previously published data <sup>7,21</sup> are provided in Table S3.  $p_{\text{CO}_2}$  and  $p_{\text{car}}$  are the CO<sub>2</sub> and carrier gas pressures, respectively. The carrier gas compositions (% N<sub>2</sub>, % CH<sub>4</sub> and % Ar) are indicated.  $T$  and  $M$  are the axially averaged temperature and Mach number, respectively, with standard deviation  $\sigma$ . The Laval nozzles are referred to by their nominal Mach numbers used to design them.

$p_{\text{CO}_2}$ [Pa]	$T (\pm \sigma)$ [K]	$p_{\text{car}}$ [Pa]	% Ar	% N <sub>2</sub>	% CH <sub>4</sub>	$M (\pm \sigma)$	Nozzle
13.3	66.8 $\pm$ 1.6	13.3	34.6	15.4	-	3.7 $\pm$ 0.06	M5.2
9.3	63.7 $\pm$ 1.2	17.2	40.4	24.6	-	3.8 $\pm$ 0.04	M5.2
6.6	62.3 $\pm$ 1.3	19.9	36.5	38.5	-	3.9 $\pm$ 0.05	M5.2
5.3	61.1 $\pm$ 1.2	21.2	39.2	40.8	-	3.9 $\pm$ 0.05	M5.2
4.0	59.7 $\pm$ 1.3	22.5	42.7	42.3	-	4.0 $\pm$ 0.06	M5.2
2.7	58.7 $\pm$ 1.2	23.9	45.4	44.6	-	4.0 $\pm$ 0.05	M5.2
1.3	54.5 $\pm$ 1.0	25.2	54.2	40.8	-	4.1 $\pm$ 0.05	M5.2
0.87	51.3 $\pm$ 1.0	25.6	65.9	30.8	-	4.2 $\pm$ 0.06	M5.2
0.53	48.8 $\pm$ 1.0	26.0	72.6	25.4	-	4.2 $\pm$ 0.06	M5.2
0.49	47.5 $\pm$ 1.7	32.5	91.1	-	7.5	4.1 $\pm$ 0.10	M5.0
0.26	42.5 $\pm$ 1.6	27.7	92.2	6.9	-	4.3 $\pm$ 0.10	M5.2
0.16	40.4 $\pm$ 1.2	34.8	77.2	22.3	-	4.7 $\pm$ 0.09	M6.0
0.11	37.4 $\pm$ 1.4	34.9	86.6	13.1	-	4.7 $\pm$ 0.11	M6.0
0.081	35.2 $\pm$ 1.3	34.9	93.6	6.2	-	4.8 $\pm$ 0.10	M6.0
0.065	34.3 $\pm$ 1.0	34.9	91.4	-	8.4	4.8 $\pm$ 0.10	M6.0

### C. Correction for Incomplete Thermalization Effects in Nucleation Experiments

Classical nucleation theory was developed under the assumption that the temperatures of the monomers, clusters and any carrier gas are all the same, i.e. nucleation occurs under isothermal or fully thermalized conditions. Feder *et al.* <sup>22</sup> recognized that if the energy released by the addition of a monomer to a cluster was not efficiently removed by collisions with a carrier gas, the experimental nucleation rate  $J_{\text{exp}}$  should be reduced from the nucleation rate under fully thermalized conditions,  $J$ , as

$$J_{\text{exp}} = f \times J. \quad (\text{S3})$$

For steady-state nucleation, the thermalization factor  $f$  (also called the non-isothermal factor) is given by <sup>22</sup>

$$f = \frac{b^2}{b^2 + q^2}, \quad (\text{S4})$$

where,

$$b^2 = 2(k_B T)^2 \left( 1 + \frac{N_{\text{car}}}{N_1} \sqrt{\frac{m}{m_{\text{car}}}} \right), \quad (\text{S5})$$

is the mean square energy fluctuation between subsequent growth or decay events, and  $N_{\text{car}}/N_1$  and  $m_{\text{car}}/m$  are the number and mass ratios of carrier gas molecules to condensable monomers, respectively. (Equation S5 is derived from that presented by Feder *et al.*<sup>22</sup> assuming  $c_v = c_{v,c} = 3k_B/2$  and the ideal gas law.) Following Feder *et al.*<sup>22</sup>, the excess energy  $q$  of the critical cluster after monomer addition is given by

$$q = \Delta H_{\text{vap}} - \frac{k_B T}{2} - \frac{\partial A_n \sigma}{\partial n} \approx \Delta H_{\text{vap}} - \frac{k_B T}{2} - k_B T \ln S. \quad (\text{S6})$$

where  $\Delta H_{\text{vap}}$  is the bulk heat of vaporization for the condensing species,  $A_n$  is the surface area of a cluster containing  $n$  monomers, and  $\sigma$  is the surface tension of the condensable.

The factor  $f$  is normally used to correct theory in order to properly compare with the experimentally observed rates. In this paper we also use  $f$  to estimate the experimental nucleation

rates  $J$  that correspond to the measured onset conditions under conditions of perfect cluster thermalization. Thus,

$$J = \frac{J_{\text{exp}}}{f}. \quad (\text{S7})$$

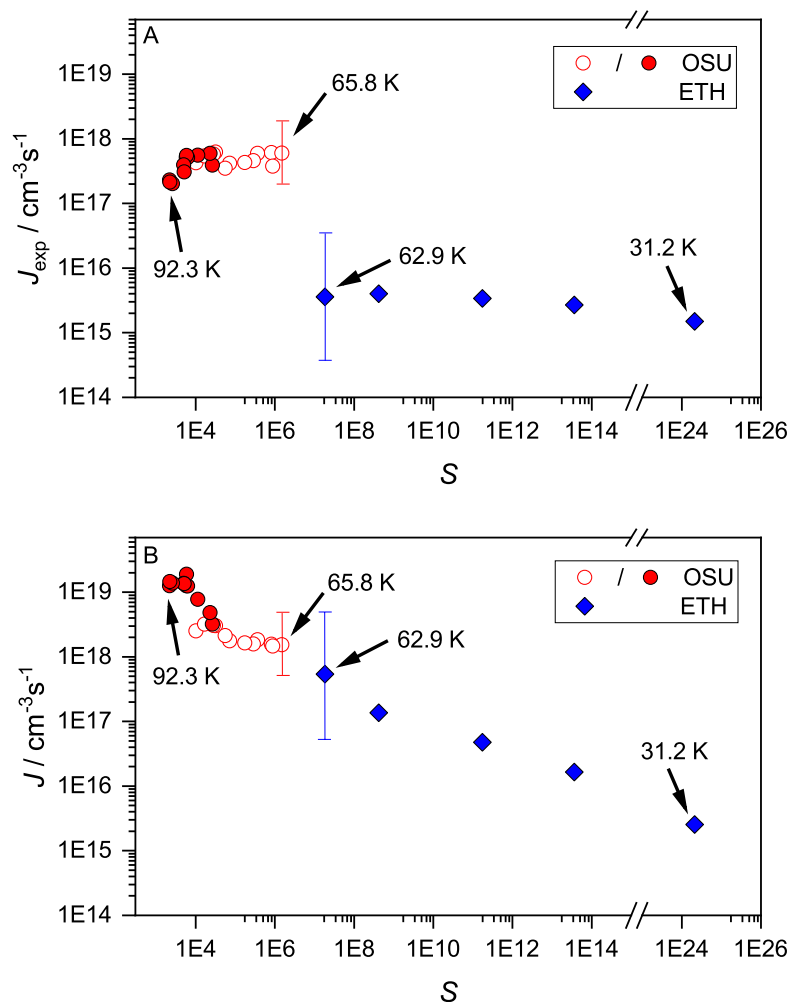
This correction is critical to fairly compare data measured under very different ratios of  $N_{\text{car}}/N_1$ . In particular, in the region of overlap, the OSU experiments typically operate at  $N_{\text{car}}/N_1 = 200$ , whereas the ETH experiments operate at  $N_{\text{car}}/N_1 \cong 1$ .

Table S1 summarizes the values of  $f$  and  $J$  corresponding to the current and previously published<sup>1</sup> values of  $J_{\text{exp}}$  measured at OSU. Table S3 summarizes the values of  $f$  and  $J$  corresponding to the previously published values of  $J_{\text{exp}}$  measured at ETH<sup>7,21</sup>.

**Table S3:** Experimental parameters for the nucleation rate measurements performed at ETH Zurich. These data have been published in refs. 7 and 21.  $p_{\text{CO}_2}$  is the  $\text{CO}_2$  pressure and  $T$  and  $M$  are the axially averaged temperature and Mach number with standard deviation  $\sigma$ , respectively.  $p_{\text{car}}$  is the carrier gas pressure and % Ar and %  $\text{CH}_4$  are the concentrations of argon and methane in the flow.  $J_{\text{exp}}$  is the experimental nucleation rate,  $f$  is the non-isothermal factor and  $J$  is the nucleation rate expected under fully thermalized conditions (see Eq. S7).

$p_{\text{CO}_2}$ [Pa]	$T$ [K ( $\pm \sigma$ )]	$p_{\text{car}}$ [Pa]	% Ar	% $\text{CH}_4$	$M (\pm \sigma)$	$J_{\text{exp}}$ [ $\text{cm}^{-3}\text{s}^{-1}$ ]	$f$	$J$ [ $\text{cm}^{-3}\text{s}^{-1}$ ]
13.3	$62.9 \pm 1.1$	13.3	42.3	7.7	$3.83 \pm 0.06$	$3.6 \times 10^{15}$	0.0066	$5.4 \times 10^{17}$
2.65	$56.6 \pm 1.3$	23.9	66.9	23.1	$4.16 \pm 0.06$	$4.0 \times 10^{15}$	0.029	$1.4 \times 10^{17}$
0.88	$49.3 \pm 1.3$	25.6	81.3	15.4	$4.65 \pm 0.07$	$3.4 \times 10^{15}$	0.072	$4.8 \times 10^{16}$
0.37	$44.4 \pm 1.5$	32.6	97.1	1.7	$4.17 \pm 0.08$	$2.7 \times 10^{15}$	0.16	$1.7 \times 10^{16}$
0.04	$31.2 \pm 1.3$	35	98.3	1.5	$4.89 \pm 0.11$	$1.5 \times 10^{15}$	0.59	$2.5 \times 10^{15}$

## S2. Further Nucleation Rate Comparisons



**Figure S1:** (A) Experimentally determined nucleation rates,  $J_{\text{exp}}$ , previously published in Dingilian *et al.*<sup>1</sup> (filled red circles), those measured as part of this work (open red circles), and the results of Krohn *et al.*<sup>7</sup> and Lippe *et al.*<sup>21</sup> (blue diamonds), exhibit distinctly different trends as a function of  $S$ . Since temperature is not constant in these experiments, the highest and lowest temperatures for each data set are indicated on the figure. All values of  $S$  are with respect to the extrapolated supercooled liquid. (B) The nucleation rates  $J = J_{\text{exp}}/f$  correspond to the rates that should be observed if nucleation occurred under fully thermalized conditions. The data now exhibit a highly consistent trend with supersaturation.

In the main body of the paper we compared the nucleation rates  $J_{\text{exp}}$  and  $J$  between the OSU and ETH experiments as a function of the pressure at onset, because  $p_{\text{CO}_2}$  and  $T$  are the parameters used in the QC calculations. Figure S1 compares  $J_{\text{exp}}$  and  $J = J_{\text{exp}}/f$  as a function of the saturation  $S = p_{\text{CO}_2}/p_{\text{CO}_2}^{\text{eq}}(T)$  where  $p_{\text{CO}_2}^{\text{eq}}(T)$  is the equilibrium vapor pressure of supercooled liquid  $\text{CO}_2$ . This comparison is insightful, because  $S$  is the driving force for nucleation and is an exponential function of  $T$ . As in Figure 3A of the main text, there is a significant gap in  $J_{\text{exp}}$  between the lowest temperature experiment measured within the nozzle (OSU data) and highest temperature experiment measured in the post-nozzle flow (ETH data) that cannot be explained by the uncertainty in either rate measurement. Rather, this difference directly reflects the difference in the degree of cluster thermalization between the two experiments in this temperature regime. In the OSU experiments, when  $T = 65.8$  K the concentration of  $\text{CO}_2$  is  $\sim 0.5$  mol % and  $f \sim 0.4$ . In contrast, in the ETH experiments, when  $T = 62.9$  K the concentration of  $\text{CO}_2 \sim 50$  mol % and  $f \sim 0.0066$ . Non-isothermal effects also play a role in the OSU experiments at higher pressures (lower saturations) where  $f \sim 0.015$  when the concentration of  $\text{CO}_2$  reaches  $\sim 39$  mol %.

After all of the nucleation rates are corrected for differences in thermalization, the values of  $J$  are quite consistent between the two experiments and both exhibit a trend of decreasing nucleation rates as the temperature decreases and supersaturation increases.

### S3. Modelling Details

#### A. Kinetic Model for Cluster Growth

As the observed nucleation occurs in a confined region in the absence of physical boundaries and pre-existing particles, external losses of monomers or clusters can be ignored. In addition, recent large-scale molecular dynamics simulations of homogenous nucleation of CO<sub>2</sub> confirm that cluster-cluster collisions are extremely rare at conditions close to those of the experiments<sup>1</sup>. Consequently, the growth mechanism is restricted to the addition or removal of monomers and the time development of the cluster concentration can be calculated using the Becker–Döring model<sup>23</sup>

$$\frac{\partial N_n}{\partial t} = \beta_{n-1}N_{n-1} + \gamma_{n+1}N_{n+1} - \beta_n N_n - \gamma_n N_n, \quad (\text{S8})$$

where  $\gamma_n$  and  $\beta_n$  are  $n$ -cluster's evaporation and collision rates, respectively.

According to kinetic gas theory, the hard sphere collision rate between a monomer and an  $n$ -cluster is (see ref. 24)

$$\beta_n = N_1 \sqrt{\frac{8\pi k_B T}{\mu}} (r_1 + r_n)^2, \quad (\text{S9})$$

where,  $N_1$  is the monomer concentration,  $\mu = n \cdot m / (n + 1)$  is the reduced mass where  $m$  is the mass of a monomer. The radii are calculated from the molecular volume  $v = m/\rho$  as  $r_n = (3nv/4\pi)^{1/3}$ , where the density of CO<sub>2</sub> bulk was used.

If the monomer concentration  $N_1$  is constant, the steady-state solution of Eq. S8 leads to the classical expression for the isothermal nucleation/growth rate  $J_{\text{iso}}$

$$J_{\text{iso}} = \left( \sum_{n=1} \frac{1}{S^n \beta_n N_n^{\text{eq}}} \right)^{-1}, \quad (\text{S10})$$

where the cluster density of an  $n$ -mer at equilibrium vapor pressure is given by <sup>25</sup>

$$N_n^{\text{eq}} = N^{\text{eq}} \exp \left( -\frac{\Delta G_n^{\text{eq}}}{k_B T} \right) = \frac{N_1}{S} \exp \left( -\frac{\Delta G_n^{\text{eq}}}{k_B T} \right), \quad (\text{S11})$$

and  $\Delta G_n$  is the cluster Gibbs free energy of formation calculated using QC methods as described in Section S3.B and C.

To account for incomplete thermalization of the clusters, a factor  $f'$  is calculated using Eq. S4 with the following modification (relative to the calculation of  $f$ ). Since both energy and momentum are conserved, a size-dependent  $q$  can be calculated using the ground-state energies ( $U_n = E_n + \text{ZPE}_n$ , where  $E$  and ZPE are electronic and zero-point energies, respectively) of adjacent clusters and the principle of equipartition as

$$q_n = U_{n-1} + U_1 - U_n - \frac{5}{2} k_B T. \quad (\text{S12})$$

For the case of dimer formation ( $n = 2$ ), the last term of Eq. S12 is  $-2k_B T$  as an additional rotational degree of freedom is introduced. The main qualitative difference between Eqs. S6 and S12, is that Eq. S6 incorrectly includes entropic contribution to  $q$  as surface tensions i.e. surface free energy is used instead of surface energy. Using  $b$  defined already in Eq. S5, the non-isothermal factor  $f'$  for a given cluster size can be expressed as (see similarity with Eq. S4)

$$f' = \frac{b^2}{b^2 + q_n^2}, \quad (\text{S13})$$

The differences between  $f$  and  $f'$  are generally on the order of 0.5-10.

The calculated formation free energies at reference pressure  $p^{\text{ref}}$  can be converted to any pressure  $p$  using following relation

$$\Delta G_n(p) = \Delta G_n^{\text{ref}} + (n - 1)RT \ln\left(\frac{p^{\text{ref}}}{p}\right), \quad (\text{S14})$$

and, thus, we can write the non-isothermal nucleation rate  $J_{\text{noniso}}$  in terms of reference pressure as

$$J_{\text{noniso}} = f' \left( \sum_{n=1} \frac{\exp\left(\left(\Delta G_n^{\text{ref}} + (n-1)RT \ln\left(\frac{p^{\text{ref}}}{p}\right)\right)/k_B T\right)}{N_1 \beta_n} \right)^{-1}. \quad (\text{S15})$$

Eq. S15 reduces to the correct kinetic limit equation as the free energy barrier vanishes. In particular, once  $p/p_{\text{ref}}$  increases enough (i.e.  $\Delta G_n \ll 0$  for  $n > 1$ ) and  $q = 0$ , the hard sphere nucleation rate neglecting evaporation,  $J_{\text{HS}}$ , is reached

$$J_{\text{HS}} = \beta_1 N_1. \quad (\text{S16})$$

$J_{\text{HS}}$  is a simplest form of the nucleation rate, i.e. coagulation and evaporation is neglected and every collision leads to association (with unit sticking probability). It is also referred to as the collisional limit and is often used as an estimate of the upper limit of the nucleation rate.



## B. Configurational Sampling

The search for the energy minimum configurations of the CO<sub>2</sub> clusters is based on the study of Kubečka *et al.*<sup>26</sup> and was performed as follows.

### **Exploration**

First, the artificial bee colony (ABC) algorithm implemented in the ABCcluster program<sup>27-28</sup> was used to explore the potential energy surface (PES). For that, the CO<sub>2</sub> geometry was optimized at the MP2/6-31+G(d) level, and the required Lennard-Jones parameters and the atomic charges were assigned from the CHARMM force field<sup>29</sup>. For each search, 1000 initial random structures (bee colony population), 500 loops (generations) and a maximum structure lifetime of 4 loops were applied to obtain at maximum 1000 of the lowest-lying energy minima structures.

### **Reoptimization**

All the saved structures were reoptimized using the semi-empirical GFN2-xTB method (the XTB program<sup>30-31</sup>) with very tight optimization criterion.

### **Removing redundant structures**

The redundant structures converging to the same configuration were removed and only unique structures were kept for further calculations. The configurations were considered unique if at least one of the collective variable's difference was greater than a predefined threshold (coll. variable [threshold]:  $E$  = energy [0.0001 Hartree],  $R_g$  = gyration radius [0.01 Å],  $\mu$  = dipole moment [0.1 D]). Moreover, all structures with energies greater than  $3.5 \cdot n$  kcal/mol with respect to the global minimum were removed as well, where  $n$  is the number of CO<sub>2</sub> molecules in the cluster.

## C. Quantum Chemical Calculations

### **Geometry**

The CO<sub>2</sub> molecule was analyzed using several levels of theory and several of the essential calculated geometrical and vibrational properties were compared to experimental results. Table S4 summarizes the obtained C—O bond distances, O—C—O angles, rotational constants and electric dipole polarizabilities, and Table S5 summarizes the vibrational frequencies of the normal modes of a CO<sub>2</sub> molecule. These CO<sub>2</sub> molecule properties are accurately determined from experiments. Our assumption is that methods describing these properties well are also likely to accurately predict properties, such as the cluster binding energy, that are not experimentally well constrained. As the results indicate, the  $\omega$ B97X-D/6-31+G(d) outperforms the other levels of theory in the category of structural features, and also represents the normal modes frequencies relatively well. This functional was also recently reported in several studies of molecular clusters to provide acceptable geometries.<sup>26, 32-33</sup> Thus, we decided to use the  $\omega$ B97X-D/6-31+G(d) method for geometry optimization and thermodynamic calculations. Moreover, the  $\omega$ B97X-D<sup>34</sup> functional is suitable for systems interacting via dispersion interactions, which are the dominating interactions in CO<sub>2</sub> clusters. If not otherwise specified, all quantum chemistry calculations were performed using Gaussian 16 Revision A.03.<sup>35</sup>

Consequently, the obtained local minimum structures from the configurational exploration were optimized using density functional theory (DFT) with very tight optimization criterion and the  $\omega$ B97X-D<sup>34</sup> functional with the 6-31+G(d) basis (example structures in Figure S2).

**Table S4:** Data validation for CO<sub>2</sub> molecule: C—O bond distance  $r_{\text{C-O}}$ , O—C—O angle  $\angle(\text{OCO})$  and rotational constant  $R$  (exp.: refs. 36-37), and electric dipole polarizability  $\alpha$  (exp.: refs. 37-38). The difference between theoretical and experimental values is noted in parentheses.

	$r_{\text{C-O}}$ [Å]	$\angle(\text{OCO})$ [°]	$R$ [cm <sup>-1</sup> ]	$\alpha$ [Å <sup>3</sup> ]
Experimental	1.162	180.0	0.3902	2.507
$\omega\text{B97X-D/6-31+G(d)}$	1.165 (0.26 %)	180.0 (0.0 %)	0.3884 (0.46 %)	2.503 (0.2 %)
$\omega\text{B97X-D/aug-cc-pVTZ}$	1.156 (0.52 %)	180.0 (0.0\%)	0.3940 (0.97 %)	1.935 (22.8 %)
MP2/aug-cc-pVTZ	1.170 (0.69 %)	180.0 (0.0\%)	0.3848 (1.38 %)	2.227 (11.2 %)
CISD/aug-cc-pVTZ	1.151 (0.95 %)	180.0 (0.0\%)	0.3980 (2.00 %)	---

**Table S5:** Data validation for normal mode vibrations of CO<sub>2</sub> molecule (exp.: refs. 36-37). The difference between theoretical and experimental values is noted in parentheses.

	Asymmetric stretch [cm <sup>-1</sup> ]	Symmetric stretch [cm <sup>-1</sup> ]	Bending [cm <sup>-1</sup> ]
Experimental	2349	1333	667
$\omega\text{B97X-D/6-31+G(d)}$	2332.9 (0.68 %)	1323.9 (0.69 %)	630.2 (5.52 %)
$\omega\text{B97X-D/aug-cc-pVTZ}$	2338.4 (0.45 %)	1337.1 (0.31 %)	656.9 (1.52 %)
MP2/aug-cc-pVTZ	2288.5 (2.57 %)	1263.5 (5.22 %)	628.0 (5.85 %)
CISD/aug-cc-pVTZ	2406.6 (2.45 %)	1393.0 (4.50 %)	696.4 (4.41 %)

## Electronic energy

The accuracy of the cluster formation energies was increased by performing single-point energy calculation on the geometries obtained at the  $\omega\text{B97X-D/6-31+G(d)}$  level using the Domain-based Local Pair Natural Orbital Coupled Cluster DLPNO-CCSD(T) method with the Tight Pair Natural Orbital (TightPNO) criterion<sup>39-41</sup> and the aug-cc-pVTZ basis set<sup>42-43</sup>. This approach has been successfully applied in several studies of molecular clusters, for example refs. 26, 32-33. DLPNO-CCSD(T) are the only quantum chemistry calculations performed with the Orca program version 4.0.1.2.<sup>44-45</sup> Further in the text, we refer to this electronic energy correction as DLPNO-CCSD(T)/aug-cc-pVTZ// $\omega\text{B97X-D/6-31+G(d)}$ .

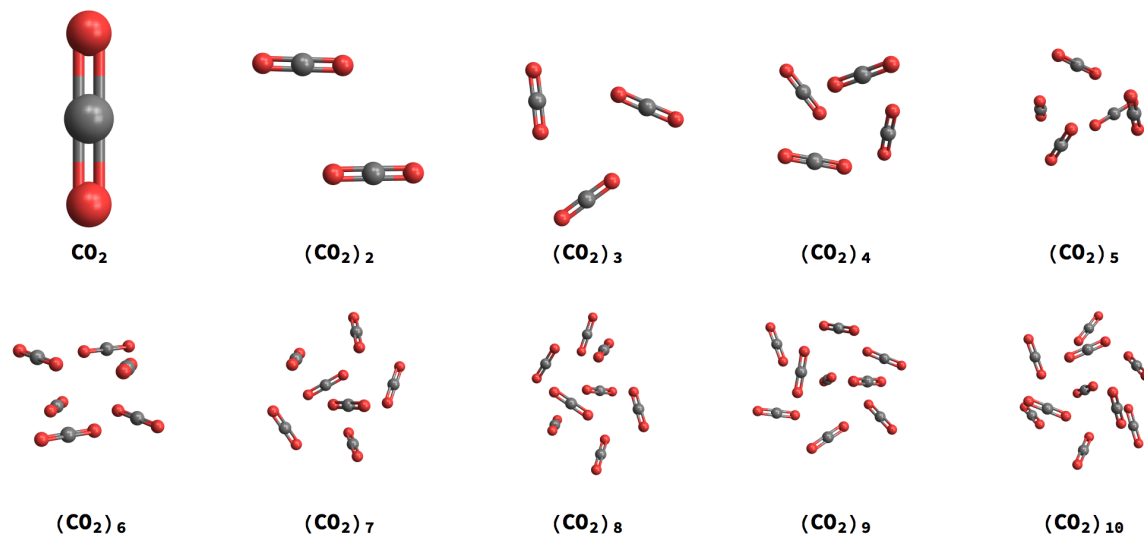


**Figure S2:** Global Gibbs-free-energy minimum structures (at 75 K) for  $\text{CO}_2$  molecule and its molecular clusters. Note that here we present only the global minimum structures but in the calculations of cluster Gibbs free energies, we account for several other local minima using equation S18.

## Thermodynamics

Vibrational frequency analysis was performed at the  $\omega\text{B97X-D/6-31+G(d)}$  level. All minima were tested for non-imaginary frequencies and their vibrational frequencies were recalculated with respect to the following phenomena: (1) Rotational symmetry: only rotational symmetry is included in this work. Quantum chemistry programs can usually recognize the point group of a molecule or few molecules, but, when it comes to molecular clusters, symmetry may not be recognized correctly due to the numerical precision of calculations (i.e., clusters are incorrectly assigned as being non-symmetrical). We therefore utilized the SYMMOL program.<sup>46</sup> The global minima configurations shown in Figure S2 should have the following point groups and symmetry numbers:  $\text{CO}_2$  ( $D_{\infty\text{h}}$ ,  $\sigma = 2$ ),  $(\text{CO}_2)_2$  ( $C_{2\text{h}}$ ,  $\sigma = 2$ ),  $(\text{CO}_2)_3$  ( $C_{3\text{h}}$ ,  $\sigma = 3$ ), and  $(\text{CO}_2)_6$  ( $S_6 = C_{3\text{i}}$ ,  $\sigma = 3$ ). It

should be noted that including the correct symmetry number has only a minor effect on the nucleation rates if the monomer symmetry is correct. (2) Quasi-harmonic approximation: the low vibrational frequencies were treated as suggested by Grimme *et al.*<sup>47</sup> and Chon *et al.*<sup>48</sup> using the GoodVibes program<sup>49-50</sup> (i.e. vibrational partition function for vibrations lower than  $0.5k_B T$  cm<sup>-1</sup> were replaced by rotational partition function and the low and high vibration expressions close to the cutoff frequency were interpolated by a damping function). (3) Vibrational anharmonicity: to account for vibrational anharmonicity, we applied a scaling factor of 0.952 (for  $\omega$ B97X-D/6-31+G(d)) to all vibrations of CO<sub>2</sub> and CO<sub>2</sub> clusters.<sup>36</sup>

Gibbs Free Energy: To obtain the Gibbs free energy  $G$  of each molecular configuration, the thermal correction  $g_{\text{corr}}^{\text{DFT}}$  (including zero-point energy (ZPE)) has to be added to the corrected electronic energy  $E_{\text{el}}^{\text{DLPNO}}$

$$G = E_{\text{el}}^{\text{DLPNO}} + g_{\text{corr}}^{\text{DFT}}. \quad (\text{S17})$$

It should be noted that  $g_{\text{corr}}^{\text{DFT}}$  is a function of temperature. Figure S2 shows the global minima of all CO<sub>2</sub> clusters at 75 K.

The most import point is to obtain the Gibbs free energy of the global minimum. However, in this study, we also included the contribution of several low-lying local minima to the Gibbs free energy. For this purpose, the equation suggested in ref. 51 was used:

$$\langle G \rangle = -RT \ln \left( \sum_i e^{-G_i/RT} \right), \quad (\text{S18})$$

where  $R$  is the universal gas constant and  $T$  is temperature.

(Original) Formation Gibbs Free Energy: In order to understand the stability of CO<sub>2</sub> clusters, formation Gibbs free energies were calculated. The Gibbs free energy of formation  $\Delta G_n$  of the cluster containing  $n$  CO<sub>2</sub> molecules is calculated from the cluster Gibbs free energy  $G_n$  (or  $\langle G_n \rangle$ ) and the Gibbs free energy of single CO<sub>2</sub> molecules  $G_1$ :

$$\Delta G_n = G_n - nG_1 \quad (\text{S19})$$

Based on the monomer benchmarking, we decided to calculate the thermal correction at  $\omega$ B97X-D/6-31+G(d). Keeping the  $\omega$ B97X-D/6-31+G(d) geometrical structures, electronic binding energies were calculated at higher levels of theory. The  $\Delta G_n$  values calculated at the DLPNO-CCSD(T)/aug-cc-pVTZ// $\omega$ B97X-D/6-31+G(d) level will be addressed as the “original” data in the following sections.

**Table S6:** Formation energies calculated at various levels of theory for global minimum structures of (CO<sub>2</sub>)<sub>1-3</sub> clusters, where  $\Delta E$  represents electronic binding energy and  $g_c$  represents thermal correction to  $E$  at 70 K ( $g_c$  contains zero-point energy (ZPE)).

	$\Delta E$ (kcal/mol)		$\Delta g_c$ (kcal/mol)	
	(CO <sub>2</sub> ) <sub>2</sub>	(CO <sub>2</sub> ) <sub>3</sub>	(CO <sub>2</sub> ) <sub>2</sub>	(CO <sub>2</sub> ) <sub>3</sub>
DLPNO-CCSD(T)/aug-cc-pVTZ// $\omega$ B97X-D/6-31+G(d)	-1.46	-4.25	1.34	3.33
CCSD(T)/aug-cc-pVTZ// $\omega$ B97X-D/aug-cc-pVTZ	-1.49	-4.13	1.30	3.24
CCSD(T)/aug-cc-pVTZ// $\omega$ B97X-D/6-31+G(d)	-1.53	-4.40	1.34	3.33
CCSD(T)/aug-cc-pVTZ+BSSE// $\omega$ B97X-D/6-31+G(d)	-1.27	-3.56	1.34	3.33

(Adjusted) Formation Gibbs Free Energy: To modify the Gibbs free energy profiles using higher level data, we calculated the energy of CO<sub>2</sub> monomer, dimer and trimer at the CCSD(T)/aug-cc-pVTZ// $\omega$ B97X-D/6-31+G(d) level of theory (see Table S6 for the variation in binding energies and thermal corrections). Also, we corrected the binding energies for the basis set superposition error (BSSE).<sup>52-53</sup> We find this method to be the most reliable, and moreover, assuming these *adjusted data*, we reached a better comparison to experimental results. Due to computational cost, the remaining formation Gibbs free energies of clusters (CO<sub>2</sub>)<sub>4-10</sub> were just adjusted from the *original* data to fit the monomer, dimer and trimer formation Gibbs free energies. The adjustment was done by a scaling factor  $\zeta$  which was fitted on the (CO<sub>2</sub>)<sub>1-3</sub> clusters

$$\Delta G_n^{\text{adj}} = \Delta G_n^{\text{orig}} + \zeta \cdot (n - 1), \quad (\text{S20})$$

and then used to obtain the rest of  $\Delta G_n^{\text{adj}}$  for  $n > 3$ . Table S7 lists  $\Delta G_n$  values at a few selected experimental conditions with the *original* data and the *adjusted* data. Also, Figure 4A in the main text shows a graph for the  $\Delta G_n$  profiles for the same few selected experimental conditions.

**Table S7:**  $\Delta G_n^{\text{orig}}$  and  $\Delta G_n^{\text{adj}}$  of all studied clusters for the experimental conditions: temperature (K) and pressure (Pa). The Gibbs free energies of formation  $\Delta G_n$  are in kcal/mol. Numbers in red indicate the critical cluster size of the *adjusted* data. The last column shows the scaling  $\zeta$  factor from Eq. S20.

		T [K]	p [Pa]		CO <sub>2</sub>	(CO <sub>2</sub> ) <sub>2</sub>	(CO <sub>2</sub> ) <sub>3</sub>	(CO <sub>2</sub> ) <sub>4</sub>	(CO <sub>2</sub> ) <sub>5</sub>	(CO <sub>2</sub> ) <sub>6</sub>	(CO <sub>2</sub> ) <sub>7</sub>	(CO <sub>2</sub> ) <sub>8</sub>	(CO <sub>2</sub> ) <sub>9</sub>	(CO <sub>2</sub> ) <sub>10</sub>	$\zeta$
31.2	0.04			$\Delta G_n^{\text{orig}}$	0.00	0.10	-0.77	-2.47	-4.26	-7.05	-8.73	-11.15	-13.87	-16.59	0.31346
				$\Delta G_n^{\text{adj}}$	0.00	0.28	-0.08	-1.53	-3.01	-5.49	-6.85	-8.95	-11.37	-13.76	
49.3	0.88			$\Delta G_n^{\text{orig}}$	0.00	0.63	0.45	-0.54	-1.57	-3.57	-4.44	-6.13	-8.02	-9.97	0.31266
				$\Delta G_n^{\text{adj}}$	0.00	0.82	1.14	0.40	-0.32	-2.01	-2.56	-3.94	-5.52	-7.16	
56.6	2.65			$\Delta G_n^{\text{orig}}$	0.00	0.81	0.85	0.11	-0.67	-2.40	-2.99	-4.42	-6.02	-7.71	0.31240
				$\Delta G_n^{\text{adj}}$	0.00	0.99	1.54	1.04	0.58	-0.84	-1.11	-2.24	-3.53	-4.90	
65.8	7.14			$\Delta G_n^{\text{orig}}$	0.00	1.05	1.38	0.94	0.50	-0.88	-1.12	-2.22	-3.45	-4.78	0.31204
				$\Delta G_n^{\text{adj}}$	0.00	1.23	2.07	1.88	1.75	0.68	0.75	-0.04	-0.95	-1.98	
77.8	61.4			$\Delta G_n^{\text{orig}}$	0.00	1.17	1.71	1.48	1.29	0.19	0.20	-0.65	-1.58	-2.63	0.31162
				$\Delta G_n^{\text{adj}}$	0.00	1.36	2.40	2.41	2.53	1.74	2.07	1.54	0.91	0.17	
85.7	278			$\Delta G_n^{\text{orig}}$	0.00	1.19	1.79	1.62	1.53	0.55	0.65	-0.09	-0.92	-1.84	0.31142
				$\Delta G_n^{\text{adj}}$	0.00	1.37	2.48	2.56	2.77	2.11	2.52	2.09	1.57	0.96	
91.7	770			$\Delta G_n^{\text{orig}}$	0.00	1.19	1.84	1.71	1.67	0.78	0.95	0.26	-0.48	-1.33	0.31126
				$\Delta G_n^{\text{adj}}$	0.00	1.37	2.52	2.64	2.92	2.34	2.81	2.44	2.01	1.48	



#### D. Onset of Nucleation

To determine the pressures and temperatures corresponding to the onset of nucleation, as illustrated in Figure 2A of the main text, we solved Eq. S15 with  $f' = 1$  for fixed isothermal nucleation rates. Here the Gibbs free energies of formation ( $\Delta G_n^{\text{ref}}$ ) are calculated for all clusters at a given set of temperatures ( $T$ ). And further, for each temperature, the CO<sub>2</sub> pressure ( $p_{\text{CO}_2}$ ) is varied until the desired nucleation rate is reached. Figure 2B in the main text shows the critical cluster sizes  $n^*$  (cluster size with the highest  $\Delta G_n^{\text{ref}}$  at given condition) for the case of  $J_{\text{iso}} = 10^{15} \text{ cm}^{-3}\text{s}^{-1}$ . The values for theoretical nucleation rates  $J_{\text{iso}}$  and  $J_{\text{noniso}}$  shown in Figures 3A and 3B of the main text are summarized in Table S8. Additionally, the experimental nucleation data are also compared with  $J_{\text{HS}}$  in Figure 2A in the main text as well as Figure S3 in the next section.

**Table S8:** Parameters relevant to the QC nucleation rate calculations include the pressures (CO<sub>2</sub> pressure  $p_{\text{CO}_2}$ , carrier gas  $p_{\text{car}}$ ), temperatures, and carrier gas compositions corresponding to the values used in the experiments (Tables S1-S3, Figure 3 in main text). Results include the critical cluster size  $n^*$  and the height of the free energy barrier  $\Delta G_{n^*}^{\text{adj}}/k_{\text{B}}T$ . The non-isothermal factor  $f'$  corrects the isothermal nucleation rate  $J_{\text{iso}}$ , derived from QC calculations, for incomplete thermalization of the clusters to yield the non-isothermal nucleation rate  $J_{\text{noniso}}$ .

$p_{\text{CO}_2}$ [Pa]	$p_{\text{car}}$ [Pa]	$T$ [K]	$n^*$	$\frac{\Delta G_{n^*}^{\text{adj}}}{k_B T}$	$f'$	$J_{\text{iso}}$ [cm <sup>-3</sup> s <sup>-1</sup> ]	$J_{\text{noniso}}$ [cm <sup>-3</sup> s <sup>-1</sup> ]
0.040	35.0	31.2	2	4.54	0.8601	$1.1 \times 10^{16}$	$9.6 \times 10^{15}$
0.37	32.6	44.4	3	9.67	0.2196	$3.1 \times 10^{15}$	$6.9 \times 10^{14}$
0.88	25.6	49.3	3	11.61	0.1118	$2.4 \times 10^{15}$	$2.7 \times 10^{14}$
2.7	23.9	56.6	3	13.70	0.0551	$2.2 \times 10^{15}$	$1.2 \times 10^{14}$
7.45	1483	66.5	3	16.01	0.6106	$1.0 \times 10^{15}$	$6.2 \times 10^{14}$
7.14	1421	65.8	3	15.83	0.6049	$1.2 \times 10^{15}$	$7.4 \times 10^{14}$
10.8	1533	68.8	3	16.10	0.5478	$1.5 \times 10^{15}$	$8.4 \times 10^{14}$
13.3	1550	69.6	3	15.98	0.5060	$2.5 \times 10^{15}$	$1.3 \times 10^{15}$
13.3	13.3	62.9	3	13.41	0.0136	$6.2 \times 10^{16}$	$8.4 \times 10^{14}$
14.7	1450	67.6	3	15.08	0.4490	$1.1 \times 10^{16}$	$4.8 \times 10^{15}$
15.8	1541	70.7	3	16.03	0.4743	$2.8 \times 10^{15}$	$1.3 \times 10^{15}$
21.5	1768	73.4	5	16.71	0.2813	$2.4 \times 10^{15}$	$6.8 \times 10^{14}$
28.9	1900	75.8	5	17.69	0.2520	$2.1 \times 10^{15}$	$5.3 \times 10^{14}$
33.9	1963	76.5	5	17.61	0.2326	$3.1 \times 10^{15}$	$7.2 \times 10^{14}$
38.6	1891	75.1	5	15.95	0.1984	$1.5 \times 10^{16}$	$3.0 \times 10^{15}$
41.5	2034	79.2	5	19.09	0.2182	$1.1 \times 10^{15}$	$2.4 \times 10^{14}$
41.5	2034	78.1	5	18.19	0.2128	$2.8 \times 10^{15}$	$5.9 \times 10^{14}$
61	1769	77.8	5	16.37	0.1376	$3.0 \times 10^{16}$	$4.1 \times 10^{15}$
63	1768	78.2	5	16.63	0.1369	$2.5 \times 10^{16}$	$3.5 \times 10^{15}$
134	3526	82.0	5	16.53	0.1414	$1.3 \times 10^{17}$	$1.8 \times 10^{16}$
198	5302	82.5	5	15.35	0.1452	$8.0 \times 10^{17}$	$1.2 \times 10^{17}$
281	7049	86.0	5	16.39	0.1490	$6.2 \times 10^{17}$	$9.2 \times 10^{16}$
278	7052	85.7	5	16.26	0.1495	$6.9 \times 10^{17}$	$1.0 \times 10^{17}$
345	8815	86.2	5	15.73	0.1521	$1.8 \times 10^{18}$	$2.7 \times 10^{17}$
411	10580	87.2	5	15.67	0.1563	$2.6 \times 10^{18}$	$4.1 \times 10^{17}$
408	10583	87.6	5	15.99	0.1588	$1.9 \times 10^{18}$	$2.9 \times 10^{17}$
528	14172	88.4	5	15.46	0.1661	$5.1 \times 10^{18}$	$8.4 \times 10^{17}$
701	18399	91.9	5	16.52	0.1757	$2.5 \times 10^{18}$	$4.4 \times 10^{17}$
770	23030	91.7	5	16.00	0.1939	$5.5 \times 10^{18}$	$1.1 \times 10^{18}$
793	23207	92.3	5	16.25	0.1929	$4.3 \times 10^{18}$	$8.2 \times 10^{17}$

## S4. Comparing the Onset Data with the Hard Sphere Collision Limit and Classical Nucleation Theory

The onset trends can also be captured quite well by self-consistent classical nucleation theory (SCNT) for an appropriate range of nucleation rates, physical property choices and the assumption that the clusters are liquid-like<sup>1</sup> (Figure S3). Furthermore, the rates approach the collisional limit assuming a simple hard sphere (HS) interaction. The rapid deviation in SCNT from the HS

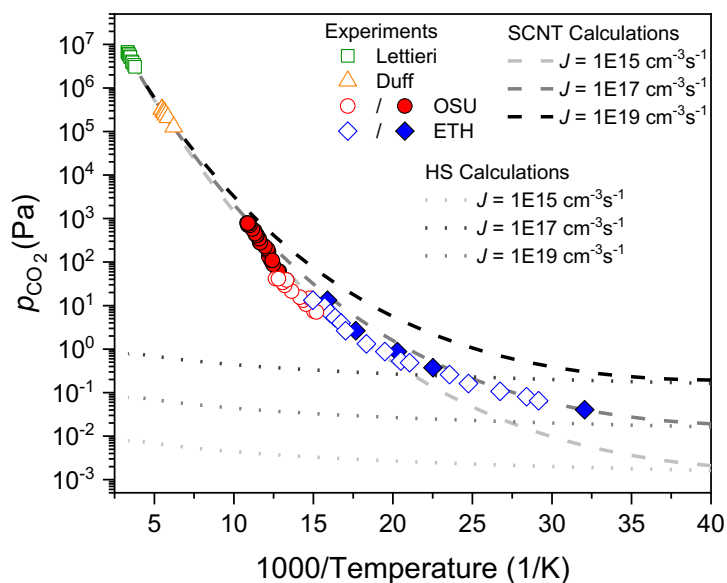


**Figure S3:** CO<sub>2</sub> partial pressure as a function of 1000/T, where data reporting the onset of nucleation are indicated by open symbols as follows: Lettieri *et al.*<sup>54</sup> (green squares), Duff<sup>55</sup> (orange triangles), OSU current work (red open circles) and ETH Zurich current work (blue diamonds). Filled symbols correspond to data from ref. 1 (red circles) and refs. 7 and 21 (blue diamonds). The data are compared with predictions by self-consistent classical nucleation theory (SCNT) and the hard sphere nucleation rate that neglects evaporation (HS). The exact expressions for the SCNT nucleation rate, and the physical properties used to evaluate it, are given in Dingilian *et al.*<sup>1</sup> In that paper we also showed that other reasonable combinations of physical property data and nucleation rate expressions were not able to match the experimental trends.

calculation particularly at temperatures above  $\sim 40$ -50 K is consistent with the appearance of a significant free energy barrier. Indications for this transition from barrierless to barrier-limited nucleation has been reported in our previous publication <sup>7</sup> and is also evident in Figure 4 of the main text.

The “straight line” region of the Volmer plot (Figure S3) can be understood within the context of classical nucleation theory as follows. Truncating the expression for stationary isothermal nucleation rate (Eq. S10) around the critical size  $n^*$  gives

$$J = S^{n^*} \beta_{n^*} Z N_{n^*}^{\text{eq}}, \quad (\text{S21})$$

where  $Z$  is the Zeldovich factor emerging from Taylor expansion of  $\Delta G_n$ , and  $n^*$  corresponds to the cluster size at the free energy maximum. The pressure  $p$  at which nucleation occurs at a given rate for a given critical cluster size  $n^*$  can then be written as

$$\ln p(n^*) = \frac{n^* - 1}{n^* + 1} \ln p^{\text{eq}} + \frac{1}{n^* + 1} \left( \ln \frac{J(RT)^2}{\beta_{n^*}' Z} + \frac{\Delta G_{n^*}^{\text{eq}}}{RT} \right), \quad (\text{S22})$$

where  $\beta_{n^*}'$  is the reduced collision coefficient ( $\beta_{n^*}'/N_1$ ). For an ideal gas, the equilibrium vapor pressure can be expressed as

$$\ln p^{\text{eq}} = \frac{-\Delta H}{T} + C_1, \quad (\text{S23})$$

where  $-\Delta H$  is the latent heat of vaporization. Thus, according to Eq. S22, for large enough critical clusters,  $\ln p$  should decrease linearly with  $1/T$ , in line with the behavior of the equilibrium vapor pressure. As the critical cluster size decreases, the second term becomes more important and the curve flattens.

## References

- (1) Dingilian, K. K.; Halonen, R.; Tikkanen, V.; Reischl, B.; Vehkamäki, H.; Wyslouzil, B. E. Homogeneous Nucleation of Carbon Dioxide in Supersonic Nozzles I: Experiments and Classical Theories. *Phys. Chem. Chem. Phys.* **2020**, *22*, 19282-19298.
- (2) Tanimura, S.; Park, Y.; Amaya, A.; Modak, V.; Wyslouzil, B. E. Following Heterogeneous Nucleation of CO<sub>2</sub> on H<sub>2</sub>O Ice Nanoparticles With Microsecond Resolution. *RSC Advances* **2015**, *5*, 105537-105550.
- (3) Park, Y.; Wyslouzil, B. E. CO<sub>2</sub> Condensation Onto Alkanes: Unconventional Cases of Heterogeneous Nucleation. *Phys. Chem. Chem. Phys.* **2019**, *21*, 8295-8313.
- (4) Ogunronbi, K. E.; Sepehri, A.; Chen, B.; Wyslouzil, B. E. Vapor Phase Nucleation of the Short-Chain *n*-Alkanes (*n*-Pentane, *n*-Hexane and *n*-Heptane): Experiments and Monte Carlo Simulations. *J. Chem. Phys.* **2018**, *148*, 144312.
- (5) Ogunronbi, K. E.; Wyslouzil, B. E. Vapor-Phase Nucleation of *n*-Pentane, *n*-Hexane, and *n*-Heptane: Critical Cluster Properties. *J. Chem. Phys.* **2019**, *151*, 154307.
- (6) Dingilian, K. K. Homogeneous Nucleation of Carbon Dioxide (CO<sub>2</sub>) in Supersonic Nozzles. Ph.D. Dissertation, Ohio State University, 2020.
- (7) Krohn, J.; Lippe, M.; Li, C.; Signorell, R. Carbon Dioxide and Propane Nucleation: The Emergence of a Nucleation Barrier. *Phys. Chem. Chem. Phys.* **2020**, *22*, 15986-15998.
- (8) Schläppi, B.; Litman, J. H.; Ferreira, J. J.; Stapfer, D.; Signorell, R. A Pulsed Uniform Laval Expansion Coupled With Single Photon Ionization and Mass Spectrometric Detection for the Study of Large Molecular Aggregates. *Phys. Chem. Chem. Phys.* **2015**, *17*, 25761-25771.
- (9) Ferreira, J. J.; Gartmann, T. E.; Schläppi, B.; Signorell, R. Can We Observe Gas Phase Nucleation at the Molecular Level? *Z. Phys. Chem.* **2015**, *229*, 1765–1780.
- (10) Ferreira, J. J.; Chakrabarty, S.; Schläppi, B.; Signorell, R. Observation of Propane Cluster Size Distributions During Nucleation and Growth in a Laval Expansion. *J. Chem. Phys.* **2016**, *145*, 211907.
- (11) Chakrabarty, S.; Ferreira, J. J.; Lippe, M.; Signorell, R. Toluene Cluster Formation in Laval Expansions: Nucleation and Growth. *J. Phys. Chem. A* **2017**, *121*, 3991-4001.

- (12) Lippe, M.; Chakrabarty, S.; Ferreiro, J. J.; Tanaka, K. K.; Signorell, R. Water Nucleation at Extreme Supersaturation. *J. Chem. Phys.* **2018**, *149*, 244303.
- (13) Li, C.; Lippe, M.; Krohn, J.; Signorell, R. Extraction of Monomer-Cluster Association Rate Constants From Water Nucleation Data Measured at Extreme Supersaturations. *J. Chem. Phys.* **2019**, *151*, 094305.
- (14) Heinbuch, S.; Dong, F.; Rocca, J. J.; Bernstein, E. R. Single Photon Ionization of Van Der Waals Clusters With a Soft X-Ray Laser:  $(\text{CO}_2)_n$  and  $(\text{CO}_2)_n(\text{H}_2\text{O})_m$ . *J. Chem. Phys.* **2006**, *125*, 154316.
- (15) Yoder, B. L.; Litman, J. H.; Forsysinski, P. W.; Corbett, J. L.; Signorell, R. Sizer for Neutral Weakly Bound Ultrafine Aerosol Particles Based on Sodium Doping and Mass Spectrometric Detection. *J. Phys. Chem. Lett.* **2011**, *2*, 2623-2628.
- (16) Litman, J. H.; Yoder, B. L.; Schlappi, B.; Signorell, R. Sodium-doping as a reference to study the influence of intracluster chemistry on the fragmentation of weakly-bound clusters upon vacuum ultraviolet photoionization. *Phys. Chem. Chem. Phys.* **2013**, *15*, 940-949.
- (17) Lengyel, J.; Pysanenko, A.; Kocisek, J.; Poterya, V.; Pradzynski, C. C.; Zeuch, T.; Slavicek, P.; Farnik, M. Nucleation of Mixed Nitric Acid-Water Ice Nanoparticles in Molecular Beams That Starts With a  $\text{HNO}_3$  Molecule. *J. Phys. Chem. Lett.* **2012**, *3*, 3096-3101.
- (18) Lengyel, J.; Pysanenko, A.; Poterya, V.; Kočišek, J.; Fárnik, M. Extensive Water Cluster Fragmentation After Low Energy Electron Ionization. *Chem. Phys. Lett.* **2014**, *612*, 256-261.
- (19) Ruberti, M.; Yun, R.; Gokhberg, K.; Kopelke, S.; Cederbaum, L. S.; Tarantelli, F.; Averbukh, V. Total Molecular Photoionization Cross-Sections by Algebraic Diagrammatic Construction-Stieltjes-Lanczos Method: Benchmark Calculations. *J. Chem. Phys.* **2013**, *139*, 144107.
- (20) Kameta, K.; Kouchi, N.; Ukai, M.; Hatano, Y. Photoabsorption, Photoionization, and Neutral-Dissociation Cross Sections of Simple Hydrocarbons in the Vacuum Ultraviolet Range. *J. Electron. Spectrosc. Relat. Phenom.* **2002**, *123*, 225-238.
- (21) Lippe, M.; Szczepaniak, U.; Hou, G.-L.; Chakrabarty, S.; Ferreiro, J. J.; Chasovskikh, E.; Signorell, R. Infrared Spectroscopy and Mass Spectrometry of  $\text{CO}_2$  Clusters During Nucleation and Growth. *J. Phys. Chem. A* **2019**, *123*, 2426-2437.
- (22) Feder, J.; Russell, K. C.; Lothe, J.; Pound, G. M. Homogeneous Nucleation and Growth of Droplets in Vapours. *Adv. Phys.* **1966**, *15*, 111-178.
- (23) Becker, R.; Döring, W. Kinetische Behandlung der Keimbildung in übersättigten Dämpfen. *Ann. Phys. (Leipzig)* **1935**, *24*, 719-752.

- (24) Seinfeld, J. H.; Pandis, S. N. *Atmospheric Chemistry and Physics: From Air Pollution to Climate Change*. 3rd ed.; John Wiley & Sons: 2016.
- (25) Courtney, W. G. Remarks on Homogeneous Nucleation. *J. Chem. Phys.* **1961**, *35*, 2249-2250.
- (26) Kubečka, J.; Besel, V.; Kurtén, T.; Myllys, N.; Vehkamäki, H. Configurational Sampling of Noncovalent (Atmospheric) Molecular Clusters: Sulfuric Acid and Guanidine. *J. Phys. Chem. A* **2019**, *123*, 6022-6033.
- (27) Zhang, J.; Dolg, M. ABCluster: The Artificial Bee Colony Algorithm for Cluster Global Optimization. *Phys. Chem. Chem. Phys.* **2015**, *17*, 24173-24181.
- (28) Zhang, J.; Dolg, M. Global Optimization of Clusters of Rigid Molecules Using the Artificial Bee Colony Algorithm. *Phys. Chem. Chem. Phys.* **2016**, *18*, 3003-3010.
- (29) Vanommeslaeghe, K.; Hatcher, E.; Acharya, C.; Kundu, S.; Zhong, S.; Shim, J.; Darian, E.; Guvench, O.; Lopes, P.; Vorobyov, I.; Mackerell Jr., A. D. CHARMM General Force Field: A Force Field for Drug-Like Molecules Compatible With the CHARMM All-Atom Additive Biological Force Fields. *J. Comput. Chem.* **2010**, *31*, 671-690.
- (30) Grimme, S.; Bannwarth, C.; Shushkov, P. A Robust and Accurate Tight-Binding Quantum Chemical Method for Structures, Vibrational Frequencies, and Noncovalent Interactions of Large Molecular Systems Parametrized for All spd-Block Elements ( $Z = 1-86$ ). *J. Chem. Theory Comput.* **2017**, *13*, 1989-2009.
- (31) Bannwarth, C.; Ehlert, S.; Grimme, S. GFN2- $\chi$ TB – An Accurate and Broadly Parametrized Self-Consistent Tight-Binding Quantum Chemical Method With Multipole Electrostatics and Density-Dependent Dispersion Contributions. *J. Chem. Theory Comput.* **2019**, *15*, 1652-1671.
- (32) Myllys, N.; Ponkkonen, T.; Passananti, M.; Elm, J.; Vehkamäki, H.; Olenius, T. Guanidine: A Highly Efficient Stabilizer in Atmospheric New-Particle Formation. *J. Phys. Chem. A* **2018**, *122*, 4717-4729.
- (33) Myllys, N.; Kubečka, J.; Besel, V.; Alfaouri, D.; Olenius, T.; Smith, J. N.; Passananti, M. Role of Base Strength, Cluster Structure and Charge in Sulfuric-Acid-Driven Particle Formation. *Atmos. Chem. Phys.* **2019**, *19*, 9753-9768.
- (34) Chai, J. D.; Head-Gordon, M. Long-Range Corrected Hybrid Density Functionals with Damped Atom-Atom Dispersion Corrections. *Phys. Chem. Chem. Phys.* **2008**, *10*, 6615-6620.
- (35) Frisch, M. J.; Trucks, G. W.; Schlegel, H. B.; Scuseria, G. E.; Robb, M. A.; Cheeseman, J. R.; Scalmani, G.; Barone, V.; Petersson, G. A.; Nakatsuji, H.; Li, X.; Caricato, M.; Marenich, A. V.;

- Bloino, J.; Janesko, B. G.; Gomperts, R.; Mennucci, B.; Hratchian, H. P.; Ortiz, J. V.; Izmaylov, A. F.; Sonnenberg, J. L.; Williams-Young, D.; Ding, F.; Lipparini, F.; Egidi, F.; Goings, J.; Peng, B.; Petrone, A.; Henderson, T.; Ranasinghe, D.; Zakrzewski, V. G.; Gao, J.; Rega, N.; Zheng, G.; Liang, W.; Hada, M.; Ehara, M.; Toyota, K.; Fukuda, R.; Hasegawa, J.; Ishida, M.; Nakajima, T.; Honda, Y.; Kitao, O.; Nakai, H.; Vreven, T.; Throssell, K.; Montgomery Jr., J. A.; Peralta, J. E.; Ogliaro, F.; Bearpark, M. J.; Heyd, J. J.; Brothers, E. N.; Kudin, K. N.; Staroverov, V. N.; Keith, T. A.; Kobayashi, R.; Normand, J.; Raghavachari, K.; Rendell, A. P.; Burant, J. C.; Iyengar, S. S.; Tomasi, J.; Cossi, M.; Millam, J. M.; Klene, M.; Adamo, C.; Cammi, R.; Ochterski, J. W.; Martin, R. L.; Morokuma, K.; Farkas, O.; Foresman, J. B.; Fox, D. J. *Gaussian 16, Revision A.03*. Gaussian Inc.: Wallingford CT, 2016.
- (36) Herzberg, G. *Molecular Spectra and Molecular Structure: II. Infrared and Raman Spectra of Polyatomic Molecules*. 1st ed.; D. Van Nostrand Co. Inc.: New York, USA, 1945.
- (37) Johnson III, R. D. *NIST Computational Chemistry Comparison and Benchmark Database, NIST Standard Reference Database Number 101*. Data retrieved from <http://www.cccbdb.nist.gov/>. 2019.
- (38) Olney, T. N.; Cann, N. M.; Cooper, G.; Brion, C. E. Absolute Scale Determination for Photoabsorption Spectra and the Calculation of Molecular Properties Using Dipole Sum-Rules. *Chem. Phys.* **1997**, *223*, 59-98.
- (39) Riplinger, C.; Neese, F. An Efficient and Near Linear Scaling Pair Natural Orbital Based Local Coupled Cluster Method. *J. Chem. Phys.* **2013**, *138*, 034106.
- (40) Riplinger, C.; Pinski, P.; Becker, U.; Valeev, E. F.; Neese, F. Sparse Maps – A Systematic Infrastructure for Reduced-Scaling Electronic Structure Methods. II. Linear Scaling Domain Based Pair Natural Orbital Coupled Cluster Theory. *J. Chem. Phys.* **2016**, *144*, 024109.
- (41) Riplinger, C.; Sandhoefer, B.; Hansen, A.; Neese, F. Natural Triple Excitations in Local Coupled Cluster Calculations With Pair Natural Orbitals. *J. Chem. Phys.* **2013**, *139*, 134101.
- (42) Dunning Jr., T. H. Gaussian Basis Sets for Use in Correlated Molecular Calculations. I. The Atoms Boron Through Neon and Hydrogen. *J. Chem. Phys.* **1989**, *90*, 1007-1023.
- (43) Kendall, R. A.; Dunning Jr., T. H.; Harrison, R. J. Electron Affinities of the First-Row Atoms Revisited. Systematic Basis Sets and Wave Functions. *J. Chem. Phys.* **1992**, *96*, 6796-6806.
- (44) Neese, F. The ORCA Program System. *WIREs Comput. Mol. Sci.* **2012**, *2*, 73-78.



- (45) Neese, F. Software Update: The ORCA Program System, Version 4.0. *WIREs Comput. Mol. Sci.* **2018**, *8*, e1327.
- (46) Pilati, T.; Forni, A. SYMMOL: A Program to Find the Maximum Symmetry Group in an Atom Cluster, Given a Prefixed Tolerance. *J. Appl. Crystallogr.* **1998**, *31*, 503-504.
- (47) Grimme, S. Supramolecular Binding Thermodynamics by Dispersion-Corrected Density Functional Theory. *Chem. Eur. J.* **2012**, *18*, 9955-9964.
- (48) Chon, N. L.; Lee, S.-H.; Lin, H. A Theoretical Study of Temperature Dependence of Cluster Formation From Sulfuric Acid and Ammonia. *Chem. Phys.* **2014**, *433*, 60-66.
- (49) Funes-Ardoiz, I.; Paton, R. S. GoodVibes: GoodVibes v1.0.1 (Version 1.0.1). 2016.
- (50) Luchini, G.; Alegre-Requena, J. V.; Funes-Ardoiz, I.; Paton, R. S. GoodVibes: Automated Thermochemistry for Heterogeneous Computational Chemistry Data. *FI1000Research* **2020**, *9*, 291.
- (51) Partanen, L.; Vehkamäki, H.; Hansen, K.; Elm, J.; Henschel, H.; Kurtén, T.; Halonen, R.; Zapadinsky, E. Effect of Conformers on Free Energies of Atmospheric Complexes. *J. Phys. Chem. A* **2016**, *120*, 8613-8624.
- (52) Boys, S. F.; Bernardi, F. The Calculation of Small Molecular Interactions by the Differences of Separate Total Energies. Some Procedures With Reduced Errors. *Mol. Phys.* **1970**, *19*, 553-566.
- (53) Simon, S.; Duran, M.; Dannenberg, J. J. How Does Basis Set Superposition Error Change the Potential Surfaces for Hydrogen-Bonded Dimers? *J. Chem. Phys.* **1996**, *105*, 11024-11031.
- (54) Lettieri, C.; Paxson, D.; Spakovszky, Z.; Bryanston-Cross, P. Characterization of Nonequilibrium Condensation of Supercritical Carbon Dioxide in a De Laval Nozzle. *J. Eng. Gas Turb. Power* **2018**, *140*, 041701.
- (55) Duff, K. M. Non-Equilibrium Condensation of Carbon Dioxide in Supersonic Nozzles. Thesis, Massachusetts Institute of Technology, 1966.